

A Model-Independent Precision Test of General Relativity using Bright Standard Sirens from ongoing and upcoming detectors

Samsuzzaman Afroz ¹*, Suvodip Mukherjee ¹

¹Department of Astronomy and Astrophysics, Tata Institute of Fundamental Research, Mumbai 400005, India

Accepted XXX. Received YYY; in original form ZZZ

ABSTRACT

Gravitational waves (GWs) provide a new avenue to test Einstein’s General Relativity (GR) using the ongoing and upcoming GW detectors by measuring the redshift evolution of the effective Planck mass proposed by several modified theories of gravity. We propose a model-independent, data-driven approach to measure any deviation from GR in the GW propagation effect by combining multi-messenger observations of GW sources accompanied by EM counterparts, commonly known as bright sirens (Binary Neutron Star(BNS) and Neutron Star Black Hole systems(NSBH)). We show that by combining the GW luminosity distance measurements from bright sirens with the Baryon Acoustic Oscillation (BAO) measurements derived from galaxy clustering, and the sound horizon measurements from the Cosmic Microwave Background (CMB), we can make a data-driven reconstruction of deviation of the variation of the effective Planck mass (jointly with the Hubble constant) as a function of cosmic redshift. Using this technique, we achieve a precise measurement of GR with redshift (z) with a precision of approximately 7.9% for BNSs at redshift $z=0.075$ and 10% for NSBHs at redshift $z=0.225$ with 5 years of observation from LVK network of detectors. Employing CE&ET for just 1 year yields the best precision of about 1.62% for BNSs and 2% for NSBHs at redshift $z=0.5$ on the evolution of the frictional term, and a similar precision up to $z=1$. This measurement can discover potential deviation from any kind of model that impacts GW propagation with ongoing and upcoming observations.

Key words: Gravitational waves, gravitation, cosmology: observations

1 INTRODUCTION

The General Theory of Relativity (GR) has stood as a cornerstone of our understanding of gravity for over a century. It elegantly explains how massive objects warp the fabric of spacetime, causing other objects to move along curved trajectories. However, in extreme astrophysical environments such as black holes and the early universe, the GR faces challenges in its applicability (Thorne 1995; Sathyaprakash & Schutz 2009). Recently, a groundbreaking development occurred with the direct detection of gravitational waves (GWs) by the LIGO-Virgo collaboration (Abbott et al. 2016b,c; Scientific et al. 2017; Abbott et al. 2017a; Goldstein et al. 2017). This achievement has opened a new avenue for testing GR, particularly in the context of compact binary systems existing in relativistic regimes. These systems include Binary Neutron Stars (BNS), Neutron Star-Black Hole pairs (NSBH), and Binary Black Holes (BBH). These compact binaries offer unprecedented opportunities to delve into the fundamental nature of gravity across a vast range of mass scales and cosmological distances. Ground-based detectors like LIGO (Aasi et al. 2015), Virgo (Acernese et al. 2014) and KAGRA (Akutsu et al. 2021) have played pivotal roles in this endeavor. Furthermore, the prospect of future space-based detectors such as LISA (Amaro-Seoane et al. 2017) and ground-based detectors such as LIGO-Aundha (LIGO-India)

(Saleem et al. 2021)¹, Cosmic Explorer(CE) (Reitze et al. 2019), and the Einstein Telescope(ET) (Punturo et al. 2010) holds even greater promise for advancing our understanding of gravity and rigorously testing GR’s predictions. Through these combined efforts, we aim to refine and expand our comprehension of the intricate interplay between gravity and the cosmos. While various models proposing modifications to the theory of gravity have been put forth to address different scenarios, this study is dedicated to testing GR in the propagation of GW through a model-independent, data-driven approach. GWs and EM signals’ propagation speed and luminosity distance offer insight into modified gravity theories. Factors like graviton mass, frictional term(due to running effect of Planck mass) and anisotropic source term contribute to deviations (Deffayet & Menou 2007; Salata et al. 2014; Nishizawa 2018; Belgacem et al. 2018a,b; Lombriser & Taylor 2016; Lombriser & Lima 2017). Precise measurements enable rigorous testing of these alternative theories. Employing bright sirens that emit both GW and EM radiation provides a robust avenue for conducting meticulous assessments of GW propagation speed, graviton mass, and the frictional term($\gamma(z)$, see in Equation.2). The prompt measurement of the electromagnetic counterpart, occurring approximately 1.7 seconds after the BNS event GW170817, has facilitated the imposition of exceedingly precise constraints on the speed of gravitational wave propagation and the mass of the graviton (Abbott et al. 2017a,b, 2019a).

Various model-dependent parametrizations of $\gamma(z)$ exist in the

* samsuzzaman.afroz@tifr.res.in

† suvodip.mukherjee@tifr.res.in

¹ <https://dcc.ligo.org/LIGO-M1100296/public>

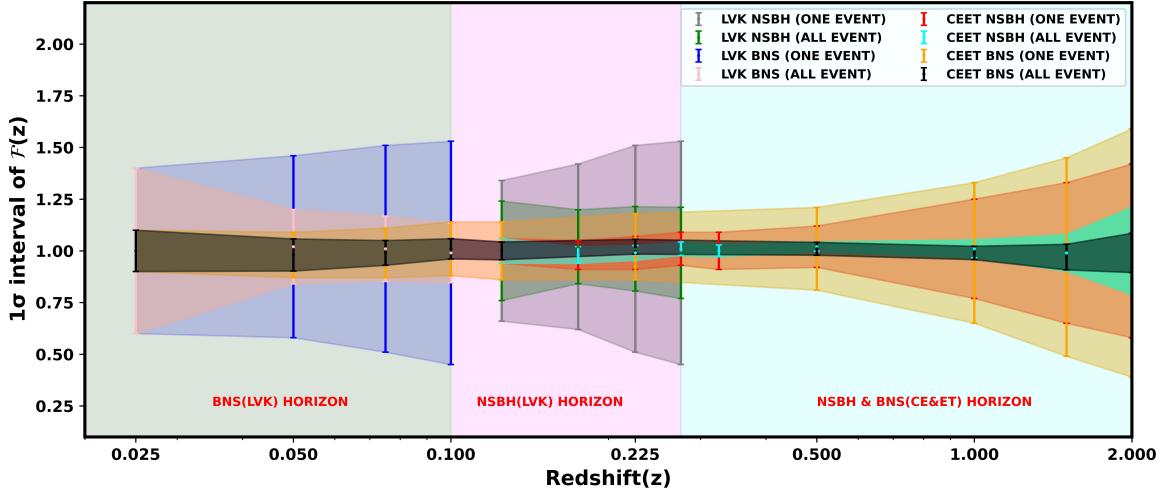


Figure 1. This plot showcases the precision achievable in reconstructing the redshift variation of the Planck mass captured by $\mathcal{F}(z)$ for both NSBH and BNS systems, employing the current LVK detector with 5 years of observation time and the future CE&ET detectors with 1 year of observation time. For LVK, the BNS case considers the total events corresponding to a local merger rate $R_0 = 500 \text{ Gpc}^{-3}\text{yr}^{-1}$, while for NSBH, $R_0 = 20 \text{ Gpc}^{-3}\text{yr}^{-1}$. For CE&ET, the BNS scenario assumes $R_0 = 100 \text{ Gpc}^{-3}\text{yr}^{-1}$, and for NSBH, $R_0 = 20 \text{ Gpc}^{-3}\text{yr}^{-1}$ are used. The plot illustrates the enhanced accuracy in measuring the function $\mathcal{F}(z)$ using future detectors compared to our current instruments is possible in the redshift range 0.2 to 1 which is an interesting cosmic epoch when the acceleration of the Universe becomes important.

literature, and one such example is the (Ξ_0, n) parametrization (Belgacem et al. 2018b) and its detectability is shown for LVK (Leyde et al. 2022) and LISA (Baker & Harrison 2021). This parameterization depends on two positive parameters, denoted as Ξ_0 and n . When Ξ_0 is set to 1, it corresponds to GR. There exist several models of modified gravity, each providing predictions for the frictional term in various scenarios. One prominent category is Scalar-Tensor theories. These theories encompass a scalar degree of freedom, the dynamics of which play a pivotal role in the evolution of the universe. Among the most well-known scalar-tensor theories of gravity are the Brans–Dicke theory (Brans & Dicke 1961), f(R) gravity (Hu & Sawicki 2007) and covariant Galileon models (Chow & Khoury 2009). These belong to the broader class known as Horndeski theories. Beyond Horndeski theories, we have Degenerate Higher Order Scalar-Tensor (DHOST) theories (Frusciante et al. 2019; Crisostomi et al. 2016; Achour et al. 2016). These have been constructed and represent, thus far, the most general scalar-tensor theories that propagate a single scalar degree of freedom alongside the helicity-2 mode of a massless graviton. There are several other well known modified gravity exist in the literature such as f(Q) gravity, f(T) gravity (Cai et al. 2016), bigravity De Felice et al. (2021), gravity in some extra dimensions (Dvali et al. 2000; Yamashita & Tanaka 2014; Corman et al. 2021) and so on. In addition, there exist additional parameterizations (Belgacem et al. 2018b), with the most significant being the polynomial-exponential and exponential parameterizations.

These models exhibit variations from one another (Belgacem et al. 2019) from the power-law form which cannot be captured by Ξ_0 and n . It is worth mentioning that for this particular parametrization, the fitting formula for $\gamma(z)$ becomes less accurate in both low and high redshifts in comparison to some of the models (see for example (Deffayet & Menou 2007)). Additionally, beyond this limited range of models, the integrated effect of $\gamma(z)$ may differ from a simple power-law form in reality. As a result, it is important to be able to test

GR in a model-independent way and measure the integrated effect of $\gamma(z)$ as a function of the data.

To address these issues, we introduce a novel model-independent function, denoted as $\mathcal{F}(z)$, defined in Equation 4. This function $\mathcal{F}(z)$ is specifically designed to account for any deviation from the GR. It serves as a metric for assessing the disparity between the distances denoted $d_l^{\text{GW}}(z)$ and $d_l^{\text{EM}}(z)$ so in standard GR this $\mathcal{F}(z)=1$.

Figure 1, highlighting the enhanced precision in measuring the redshift-dependent variation of the Planck mass ($\mathcal{F}(z)$) for NSBH and BNS systems. Notably, the precision achieved is approximately 7.9% for BNS systems at redshift 0.075 and 10% for NSBH systems at redshift 0.225 over a 5-year observation period from the LVK network of detectors. Furthermore, employing CE&ET for just 1 year yields remarkable precision, reaching about 1.62% for BNS systems and 2% for NSBH systems at redshift 0.5, assuming a fixed Hubble constant. However, when considering a varying Hubble constant, the error bar increases to approximately 2 to 2.2 times that of a fixed Hubble constant. Figure 1 also emphasizes that the measurement of $\mathcal{F}(z)$ is particularly improved in the redshift range of 0.2 to 1.0. This improvement is attributed to two main factors: signal-to-noise ratio (SNR) and the number of events. For a more detailed analysis, refer to Section 6. In the (Ξ_0, n) frictional term parametrizations, Ξ_0 is set to 1 as the fiducial value. Notably, parameter which controls the redshift evolution denoted by n lacks definition at this point. Measuring n becomes challenging as Ξ_0 nears 1 (Belgacem et al. 2018b). Model-independent parametrization enables redshift scaling for $F(z)$, even for the GR value, in contrast to parametric forms.

The paper is structured as follows: In Section 2, we delve into the propagation of GW beyond GR. Subsequently, we present our proposed model-independent, data-driven reconstruction of the variation of the effective Planck mass(frictional term). In Section 3, we shift our attention to the astrophysical population of GW sources and explore their detection using both current and future detectors.

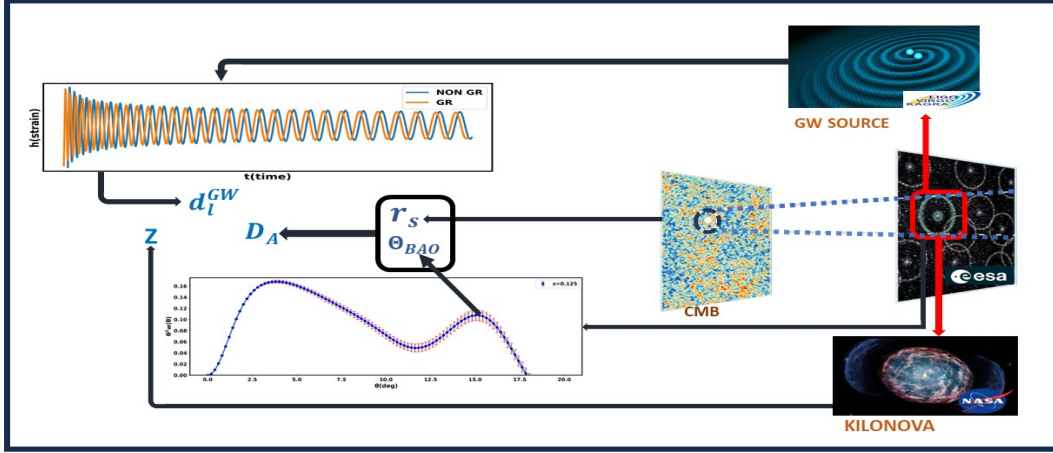


Figure 2. This is a schematic diagram demonstrates the measurement of three distinct length scales: the sound horizon (r_s), BAO scale (θ_{BAO}), and the GW luminosity distance (d_l^{GW}). These measurements are obtained from different independent observables such as CMB observations, galaxy correlation functions, and gravitational wave sources. Using this signal, we can make a data-driven test of GR as a function of redshift using Equation 6.

Section 4 is dedicated to a comprehensive discussion on the model-independent measurement of the BAO scale from the galaxy power spectrum. In Section 5, we provide a detailed exposition of the formalism underpinning our work. Moving forward, Section 6 encapsulates the main findings of our methodology, while Section 7 serves as the culmination, summarizing our key discoveries and engaging in a discourse on future prospects.

2 NON-PARAMETRIC RECONSTRUCTION OF DEVIATION FROM GENERAL RELATIVITY: FORMALISM

The propagation of GW in the fabric of spacetime, as described by the GR, can be mathematically expressed as follows

$$h_{(+,\times)}'' + 2\mathcal{H}h_{(+,\times)}' + c^2 k^2 h_{(+,\times)} = 0, \quad (1)$$

where $h_{(+,\times)}$ is GW strain of plus (+) and cross (\times) polarization, the prime symbol denotes the derivative with respect to the conformal time(η) and \mathcal{H} represents the Hubble parameter in comoving coordinates. We utilize this equation as a starting point to examine the propagation of GWs and evaluate the validity of the GR. The modified theory of gravity generalizes this equation as follows

$$h_{(+,\times)}'' + 2(1 - \gamma(z))\mathcal{H}h_{(+,\times)}' + (c_{GW}^2 k^2 + m_{GW}^2 a^2)h_{(+,\times)} = a^2 \Pi_{(+,\times)}, \quad (2)$$

In this formulation, several additional parameters come into play. Firstly, we have the frictional term denoted by $\gamma(z)$, which represents the influence of friction in the theory. The speed of GW propagation is represented by c_{GW} , a is the scale factor and the graviton mass by m_{GW} . Finally, the anisotropic stress term is denoted by $\Pi_{(+,\times)}$.

It is noteworthy that, within the framework of the GR, all these additional parameters assume a fiducial value of zero, except for c_{GW} , which corresponds to the speed of light(c). In the context of testing GR through propagation, it is essential to scrutinize the additional parameters and ascertain whether they deviate from the values predicted by GR. Recent measurements, particularly from the GW170817 event, have provided stringent constraints, indicating that the graviton mass (m_{GW}) is zero, and the speed of GW propagation

(c_{GW}) is equivalent to the speed of light (c) (Abbott et al. 2017b, 2019a).

A modification of the the anisotropic stress term ($\Pi_{+,\times}$) affects the phase of the binary waveforms; the recent BH–BH observations, in particular of GW150914 and GW151226, have set some limit on such modifications, although for the moment not very stringent Abbott et al. (2016a).

The presence of the frictional term $\gamma(z)$ changes the amplitude of the GW signal received from a source at cosmological distance. This is particularly interesting because it implies that the luminosity distance measured with standard sirens is in principle different from that measured with standard candles or other electromagnetic probes such as CMB or BAO, and this could provide a “smoking gun” signature of modified gravity. So as a consequence the GW luminosity distance d_l^{GW} is related to the electromagnetic wave-based luminosity distance d_l^{EM} by an exponential factor, where the exponent involves integrating $\gamma(z')/(1+z')$ with respect to z' (Belgacem et al. 2018a). Consequently, the expression becomes

$$d_l^{GW}(z) = \exp\left(-\int dz' \frac{\gamma(z')}{1+z'}\right) d_l^{EM}(z). \quad (3)$$

In our investigation, we focus on tensor perturbations, where the impact is encoded in the non-trivial function $d_l^{GW}(z)/d_l^{EM}(z)$. In this study, we propose a non-parametric reconstruction of the deviation from GR as

$$d_l^{GW}(z) = \mathcal{F}(z)d_l^{EM}(z). \quad (4)$$

The term $\mathcal{F}(z)$ can capture any deviation from GR as a function of redshift. The reconstruction of this quantity from observation of $d_l^{GW}(z)$ and $d_l^{EM}(z)$ can capture any modified gravity models which predict a modification in the GW propagation (Belgacem et al. 2019). Alternatively, a parametric form using Ξ_0 and n , $d_l^{GW}(z)/d_l^{EM}(z) = \Xi_0 + \frac{1-\Xi_0}{(1+z)^n}$ is also used to capture all those models which predicts a power-law modification with redshift of the GW propagation effect (Belgacem et al. 2018b).

In the realm of binary systems, GW offers a unique method for determining luminosity distance, denoted as d_l^{GW} . This distance measurement is derived from GW events. While the luminosity dis-

tance can also be determined using the standard Λ CDM cosmology, such an approach is inherently model-dependent. To obtain a model-independent data-driven inference of luminosity distance, we utilize EM luminosity distance calculations derived from various length scales.

Data-driven inference of luminosity distance: A data-driven approach to infer the luminosity distance can be made by using the BAO angular peak position (θ_{BAO}) inferred from large scale structure observation (Peebles 1973). The position of the BAO peak in the galaxy two-point correlation function can be inferred directly from observation. The angular scales are related to the comoving sound horizon until the redshift of drag epoch ($z_d \sim 1020$) as

$$r_s = \int_{z_d}^{\infty} \frac{dz c_s(z)}{H_0 \sqrt{\Omega_m(1+z)^3 + \Omega_\Lambda + \Omega_r(1+z)^4}}. \quad (5)$$

Combining these two and using the distance duality relation for EM probes, one can write the above equation as (Mukherjee et al. 2021a)

$$\mathcal{F}(z) = \frac{d_l^{\text{GW}}(z)\theta_{\text{BAO}}(z)}{(1+z)r_s}. \quad (6)$$

The comoving sound horizon r_s at the drag epoch can be related to the comoving sound horizon r_* at the redshift of recombination ($z_* = 1090$) by $r_d \approx 1.02r_*$. The quantity r_* is inferred from CMB observation, using the position of the first peak in the CMB temperature power spectrum $\theta_* = r_*/(1+z_*)D_A^{EM}(z_*)$ (Spergel et al. 2007; Komatsu et al. 2011; Hinshaw et al. 2013; Aghanim et al. 2020).

In the above equation, $d_l^{\text{GW}}(z)$ is measured from GW sources, θ_{BAO} is measured from galaxy two point correlation function, and r_s is inferred from the CMB temperature fluctuations. The redshift to the GW source can be inferred from EM counterpart for a bright stand siren. As a result, the product of all these observable quantities will lead to an identity value at all redshifts if GR and the fiducial Λ CDM model of cosmology is the correct theory. However, if there is any departure from these models, then we can measure a deviation from one with redshift. It is important to note that the value of r_s depends on the redshift above $z_d = 1020$. Though it depends on the model of cosmology, it is a redshift independent number of a constant value for the low redshifts $z < 2$. So, even if there is an inaccuracy in the inference of true r_s , the value of $\mathcal{F}(z)$ will vary by an overall normalization. But the reconstructed redshift evolution of $\mathcal{F}(z)$ will remain the same. In one of the later sections, we will show results for both the cases, (i) only $\mathcal{F}(z)$ and (ii) $\mathcal{F}(z)$ and H_0 together. The second case will make it possible to marginalise over any inaccurate inference of sound horizon r_s due to incorrect inference of the Hubble constant.

Several alternative models of GR predict deviation in different natures of the acceleration of the Universe that are predicted from the Λ CDM. As a result, this data-driven approach can make it possible to explore both deviation from GR and $w = -1$ equation of state of dark energy. The use of different observational probes was done previously (Mukherjee et al. 2021a) for a parametric form of deviation from GR (using Ξ_0 and n) valid for a class of model. However, the non-parametric form using $\mathcal{F}(z)$ proposed in this analysis, can make a redshift-dependent reconstruction of any deviation from GR using the multi-messenger observations.

The redshift can be deduced through the EM counterparts associated with these bright sirens. Ongoing and upcoming missions dedicated to identifying EM counterparts include DESI (Adame et al. 2023), Vera Rubin (Abell et al. 2009), Fermi (Bissaldi et al. 2009), Swift (Burrows et al. 2005), HST (Scoville et al. 2007), Roman space telescope (Eifler et al. 2021), Chandra (Vikhlinin et al. 2009), VLA

(Benz & Guedel 1989), ZTF (Bellm 2014), Astrosat (Agrawal 2006). A comprehensive article on the required multi-messenger observations can be found here (Ronchini et al. 2022). For the measurement of BAO scale, ongoing and upcoming missions are committed to spectroscopic surveys. Notable projects in this regard include eBOSS (Alam et al. 2017), DESI (Adame et al. 2023), Vera Rubin (Abell et al. 2009), Euclid (Laureijs et al. 2011), and SPHEREx (Doré et al. 2018). CMB measurements from the ongoing and upcoming missions include ACTPol (Thornton et al. 2016), Simons Observatory (Abitbol et al. 2019), SPT-3G (Sobrin et al. 2022) and CMB-S4 (Abazajian et al. 2016).

3 GW MOCK SAMPLES FOR LVK, COSMIC EXPLORER, AND EINSTEIN TELESCOPE

3.1 Modelling of the astrophysical population of GW source

To accurately assess deviations from the GR model, it is crucial to rely on real GW events. The total number of GW events is contingent upon the merger rates, and mass population of the GW sources. We will explain below the astrophysical models used in the analysis.

Merger rate: In this study we use a delay time model of the binary mergers (Ochsner et al. 2012; Dominik et al. 2015). In the delay time model, the merger rate is described in terms of the delay time distribution, denoted as t_d . The delay time refers to the elapsed time between the formation of stars that will eventually become black holes and the actual merging of these black holes. It is important to note that the time delay is not uniform across all binary black holes but instead follows a specific distribution. This distribution function accounts for the variations in the delay time and is defined as follows:

$$p_t(t_d|t_d^{\min}, t_d^{\max}, d) \propto \begin{cases} (t_d)^{-d} & \text{for } t_d^{\min} < t_d < t_d^{\max}, \\ 0 & \text{otherwise} \end{cases}, \quad (7)$$

The delay time is given by $t_d = t_m - t_f$, where t_m and t_f are the lookback times of merger and formation respectively (Karathanasis et al. 2023). So the merger rate at redshift z can be defined as

$$R_{\text{TD}}(z) = R_0 \frac{\int_z^{\infty} p_t(t_d|t_d^{\min}, t_d^{\max}, d) R_{\text{SFR}}(z_f) \frac{dt}{dz_f} dz_f}{\int_0^{\infty} p_t(t_d|t_d^{\min}, t_d^{\max}, d) R_{\text{SFR}}(z_f) \frac{dt}{dz_f} dz_f}, \quad (8)$$

The parameter R_0 represents the local merger rate, indicating the frequency of mergers at a redshift of $z=0$. According to the study in Abbott et al. (2023), the estimated values of R_0 for BNS systems vary between $10 \text{ Gpc}^{-3}\text{yr}^{-1}$ and $1700 \text{ Gpc}^{-3}\text{yr}^{-1}$. For NSBH systems, the R_0 values range from $7.8 \text{ Gpc}^{-3}\text{yr}^{-1}$ to $140 \text{ Gpc}^{-3}\text{yr}^{-1}$.

In our study, we assume a standard local merger rate of $R_0 = 20 \text{ Gpc}^{-3}\text{yr}^{-1}$ for NSBH systems. For BNS systems, we consider four different scenarios with R_0 values of 100, 200, 300, and 500 $\text{Gpc}^{-3}\text{yr}^{-1}$ respectively. This methodology allows us to examine the effects of different local merger rates on our results. .

The numerator of the expression involves the integration over redshift z_f from z to infinity, where $p_t(t_d|t_d^{\min}, t_d^{\max}, d)$ is the delay time distribution, $R_{\text{SFR}}(z_f)$ is the star formation rate, and $\frac{dt}{dz_f}$ is the jacobian of the transformation. The star formation rate($R_{\text{SFR}}(z)$), is determined using the Madau & Dickinson (2014) star formation rate.

The total number of compact binary coalescing events per unit redshift is estimated as

$$\frac{dN_{\text{GW}}}{dz} = \frac{R_{\text{TD}}(z)}{1+z} \frac{dv_c}{dz} T_{\text{obs}}, \quad (9)$$

where T_{obs} indicates the total observation time, $\frac{dV_c}{dz}$ corresponds to the comoving volume element, and $R(z)$ denotes the merger rate (Karathanasis et al. 2022). We consider the delay time merger rate with a specific delay time $t_d = 500$ Myrs and a power-law exponent of $d = 1$. However, it is regrettable to note that not all of these events can be detected due to the limitations imposed by the sensitivity of our current detectors. To determine which events are detectable, the calculation of the matched filtering signal-to-noise ratio (SNR) plays a crucial role. The SNR serves as a measure of the strength of the gravitational wave signal relative to the background noise. Only those events with a matched filtering SNR greater than or equal to a predetermined threshold SNR (ρ_{TH}) can be reliably detected. (Maggiore 2007)

For a GW emitted by an optimally oriented binary system, the optimized SNR, denoted as ρ , is defined as follows (Sathyaprakash & Dhurandhar 1991; Cutler & Flanagan 1994; Balasubramanian et al. 1996; Nissanke et al. 2010)

$$\rho^2 \equiv 4 \int_{f_{\min}}^{f_{\max}} df \frac{|h(f)|^2}{S_n(f)}, \quad (10)$$

Here, $S_n(f)$ represents the power spectral density of the detector. The function $h(f)$ corresponds to the Gravitational Wave (GW) strain in the restricted post-Newtonian approximation and is defined for plus (+) and cross (\times) polarization as (Ajith et al. 2008):

$$h(f)_{\{+, \times\}} = \sqrt{\frac{5\eta}{24}} \frac{(GM_c)^{5/6}}{d_L \pi^{2/3} c^{3/2}} f^{-7/6} e^{i\Psi(f)} \mathcal{I}_{\{+, \times\}}, \quad (11)$$

In this expression, the symbol η represents the symmetric mass ratio. The term M_c signifies the chirp mass of the system. The variable d_L denotes the luminosity distance. The constant c represents the speed of light in a vacuum. $\mathcal{I}_+ = (1 + \cos^2 i)/2$ and $\mathcal{I}_\times = \cos i$ depends on the inclination angle i . Finally, $\Psi(f)$ stands for the phase of the waveform. However, the signal detected by a GW detector h_{det} is a complex interplay of several variables, including the detection antenna functions (F_+ , F_\times), and can be expressed as:

$$h_{\text{det}} = F_+ h_+ + F_\times h_\times, \quad (12)$$

here F_+ and F_\times are the antenna functions defined as follows (Finn & Chernoff 1993)

$$F_+ = \frac{1}{2}(1 + \cos^2 \theta) \cos 2\phi \cos 2\psi - \cos \theta \sin 2\phi \sin 2\psi, \quad (13)$$

$$F_\times = \frac{1}{2}(1 + \cos^2 \theta) \cos 2\phi \cos 2\psi + \cos \theta \sin 2\phi \sin 2\psi,$$

where θ and ϕ define the location of the source in the sky, and ψ is related to the orientation of the binary system with respect to the detector. Consequently, the matched filtering SNR (ρ) takes the form (Finn 1996)

$$\rho = \frac{\Theta}{4} \left[4 \int_{f_{\min}}^{f_{\max}} h(f)^2 / S_n(f) df \right]^{1/2}, \quad (14)$$

where $\Theta^2 \equiv 4(F_+^2(1 + \cos^2 i)^2 + 4F_\times^2 \cos^2 i)$. Averaging over many binaries inclination angle and sky positions, Finn (1996) showed that Θ follows a distribution

$$P_\Theta(\Theta) = \begin{cases} 5\Theta(4 - \Theta)^3 / 256 & \text{if } 0 < \Theta < 4, \\ 0 & \text{otherwise.} \end{cases}$$

Mass model : The mass population used for BNS and NSBHs are motivated by the recent results from the third catalog of GW sources

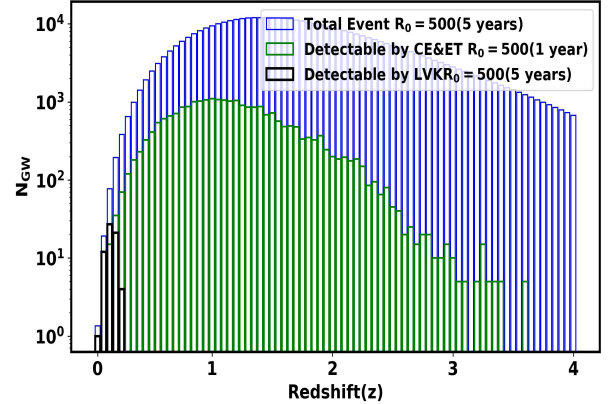


Figure 3. Total number of injected events (in blue) and the number of detectable GW events as a function of redshift for BNS sources are shown for CE&ET (in green) and LVK (in black). The total observation periods are mentioned in parentheses.

by the LVK collaboration (Abbott et al. 2023; Talbot & Thrane 2018; Abbott et al. 2019b). To model the primary mass distribution for black holes, we adopt a Power Law + Gaussian Peak model with smoothing, which combines a power law distribution with the inclusion of a Gaussian component encompassing masses ranging from $10M_\odot$ to $20M_\odot$. Conversely, we assume a uniform distribution of masses for the secondary component of the neutron star, falling within the range of $1M_\odot$ to $2M_\odot$.

In this study, we employ two sets of GW detectors: one comprising LIGO (Aasi et al. 2015), Virgo (Acernese et al. 2014) and KAGRA (Akutsu et al. 2021) (LVK), and the other consisting of Cosmic Explorer (Reitze et al. 2019) and Einstein Telescope (Punturo et al. 2010) (CE&ET).

For the LVK system, a threshold SNR of $\rho_{TH} = 12$ is chosen. For CE&ET, the threshold SNR is adjusted to enable the detection of events up to a redshift of 3 (which corresponds to an SNR of 25 and 55 for BNS and NSBH respectively.). A redshift bin size of $\Delta z = 0.025$ is adopted, and within this bin, the total number of events is computed using Equation 9. Events are generated based on distances inferred from redshifts, the parameter Θ , and object masses from their respective distributions.

For NSBH systems, the LVK's 5-year operation is projected to yield approximately 30 detectable events (all of them need not have a detectable EM counterpart). However, with a one-year observation period, the CE&ET are expected to identify around 600 events. In the case of BNS systems, the LVK's 5-year operation is anticipated to result in approximately 25, 39, and 60 detectable events for local merger rates (R_0) of 200, 300, and 500 $\text{Gpc}^{-3}\text{yr}^{-1}$ respectively. On the other hand, CE&ET are expected to detect approximately 4800 events in a one-year observation period with $R_0=100$.

In Figure 3 and Figure 4, we present the projected total and detectable coalescing events involving BNS and NSBH systems within specific redshift intervals (Δz). To obtain these estimates, we first determine the number of merging events for each redshift bin using Equation 9. For each event, we employ the inverse transform method to derive the primary mass, secondary mass, and Θ from their respective probability distributions. The primary mass is generated within the range of $10M_\odot$ to $20M_\odot$, the secondary mass within $1M_\odot$ to $2M_\odot$, and Θ within the interval 0 to 4. Incorporating redshift in-

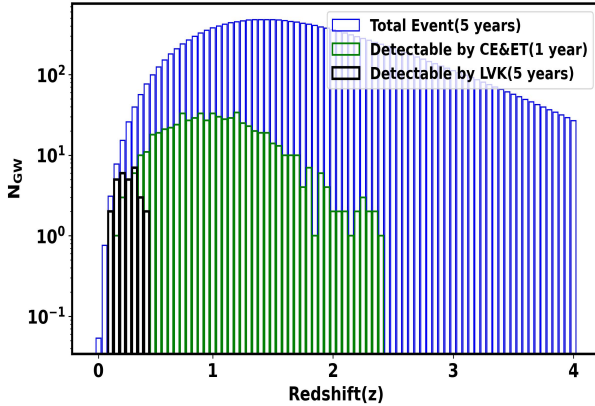


Figure 4. Total number of injected events (in blue) and the number of detectable GW events as a function of redshift for NSBH sources are shown for CE&ET (in green) and LVK (in black). The total observation periods are mentioned in parentheses.

formation for each event, we calculate the corresponding luminosity distance and SNR using Equation 14 for a single detector. The total SNR denoted as ρ_{total} , is then determined by combining individual SNRs from individual detectors using the formula $\rho_{\text{total}} = \sqrt{\sum_i \rho_i^2}$.

This detection capability is evaluated using both the CE&ET and LVK network of GW detectors over a defined observation period, T_{OBS} . The depicted curve in the graph illustrates the distribution of these events up to a redshift of $z = 4$. This representation offers valuable insights into the temporal occurrence of these mergers throughout cosmic history and the likelihood of their successful detection using current and future planned instrumentation.

3.2 GW Source Parameter Estimation using Bilby

We initiate the parameter estimation process for these discernible sources by employing the Bilby (Ashton et al. 2019) package, which yields realistic posterior distributions on the GW luminosity distance marginalized over the other source parameters. The mass of the GW sources and the number of sources with redshift are drawn as described in the last section. For the remaining source parameters, such as the inclination angle (i), polarization angle (ψ), GW phase (ϕ), right ascension (RA), and declination (Dec), we sample uniformly, considering a non-spinning system. With these injected parameters, we proceed to generate a GW signal using the IMRPhenomHM (Kalaghatgi et al. 2020) waveform model. This model incorporates higher-order modes that can alleviate the degeneracy between the luminosity distance(d_L) and inclination angle(i) for unequal mass sources. By constraining the priors of all other parameters to delta functions², we generate posterior distributions for m_1 , m_2 , d_L and i . Among these, the posterior of d_L is particularly crucial for our study, as it will be used for the inference of $\mathcal{F}(z)$. Additionally, the detection probability of the electromagnetic counterpart is contingent on the value of the inclination i (Chase et al. 2022; Ronchini et al. 2022).

² We have assumed here that the RA and Dec are inferred from the EM counterpart.

4 BARYON ACOUSTIC OSCILLATION SCALE FROM GALAXY POWER SPECTRUM

Inference of BAO from galaxy two-point angular correlation function: The BAO arises from the intricate interplay between radiation pressure and gravity during the early stages of the Universe. Previous works on this and corresponding measurements can be found here (Peebles 1973; Crocce et al. 2011). As photons and baryons decouple, a specific length known as the sound horizon at the drag epoch (z_d), represented by r_s , leaves a distinct signature on the distribution of galaxies and the power spectrum of CMB anisotropies (Peebles & Yu 1970; Sunyaev & Zeldovich 1970; Bond & Efstathiou 1987; Hu & Dodelson 2002; Blake & Glazebrook 2003). By examining the two-point angular correlation function (2PACF) of galaxy catalogs denoted by $w(\theta)$, one can identify the BAO signature, which manifests as a prominent feature resembling a bump. The BAO scale can be derived by fitting the angular correlation function $w(\theta)$ with a model defined as a combination of a power-law and a Gaussian component as (Xu et al. 2012; Carvalho et al. 2016; Alam et al. 2017)

$$w(\theta, z) = a_1 + a_2 \theta^k + a_3 \exp\left(-\frac{(\theta - \theta_{\text{FIT}}(z))^2}{\sigma_\theta^2}\right), \quad (15)$$

where, the coefficients a_i represent the parameters of the model, σ_θ denotes the width of the BAO feature, and θ_{FIT} corresponds to the best-fit value of the angular BAO scale. This signature serves as a robust standard ruler, enabling independent measurements of the angular diameter distance denoted as $d_A(z)$ (Peebles & Hauser 1974; Davis & Peebles 1983; Hewett 1982; Hamilton 1993; Landy & Szalay 1993).

Modelling of the 2PACF: Theoretically, one can model the 2PACF $w(\theta)$ as

$$w(\theta) = \sum_{l \geq 0} \left(\frac{2l+1}{4\pi} \right) P_l(\cos(\theta)) C_l, \quad (16)$$

where P_l is the Legendre polynomial of the l^{th} order and C_l the angular power spectrum, which can be expressed in terms of the three-dimensional matter power spectrum $\mathcal{P}(k)$ as follows (Peebles 1973; Crocce et al. 2011)

$$C_l = \frac{1}{2\pi^2} \int 4\pi k^2 \mathcal{P}(k) \psi_l^2(k) e^{-k^2/k_{\text{eff}}^2}, \quad (17)$$

where the quantity $\psi_l(k)$ is defined as:

$$\psi_l(k) = \int dz \phi(z) j_l(kr(z)), \quad (18)$$

where $\phi(z)$ is the galaxy selection function and j_l is the spherical Bessel function of the l^{th} order, and $r(z)$ is the comoving distance. To improve the convergence of the integral for the angular power spectrum, a damping factor $e^{(-k^2/k_{\text{eff}}^2)}$ is introduced (Anderson et al. 2012). Throughout the calculations, we adopt a fixed value of $1/k_{\text{eff}} = 3$ Mpc/h, which has no significant impact on the angular power spectrum for the scales of interest.

In this study, we calculate the matter power spectrum from the module CAMB (Lewis & Challinor 2011), and the selection function on redshift is formulated as a normalized Gaussian function. The standard deviation of this Gaussian function is set to be 5% of the mean value. The anticipated photo-z error for the Vera Rubin Observatory is described by the expression $0.03(1+z)$, as referenced in (Mandelbaum et al. 2018). Figure 5 visually demonstrates how the product of $\theta^2 w(\theta)$ changes with angular separation at a specific

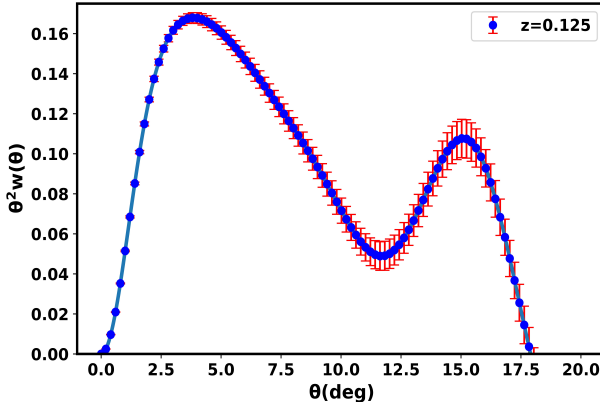


Figure 5. This plot illustrates the relationship between the 2PACF($\theta^2 w(\theta)$) is shown as a function of θ for a specific redshift, $z=0.125$ calculated using the linear matter power spectrum. Notably, a distinct bump is observed around $\theta \sim 16.0$, indicating the presence of the BAO characteristic scale θ_{BAO} .

redshift $z = 0.125$. The prominent peak at $\theta \sim 16.0$ is a significant observation, highlighting the characteristic scale associated with BAO, which is crucial for our study.

The covariance of $w(\theta)$, denoted as $Cov_{\theta\theta'}$, is modelled as

$$Cov_{\theta\theta'} = \frac{2}{f_{sky}} \sum_{l \geq 0} \frac{2l+1}{(4\pi)^2} P_l(\cos(\theta)) P_l(\cos(\theta')) \left(C_l + \frac{1}{n} \right)^2, \quad (19)$$

Here, $1/n$ is the shot noise which is related to the number density of galaxies n or, more precisely, the number of objects per steradian, and f_{sky} represents the fraction of the sky that is covered by the survey or observation (Cabré et al. 2007; Dodelson & Schmidt 2020). Figure 6 illustrates how the covariance matrix, derived from the linear matter power spectrum, changes concerning angular separations at a specific redshift. The increase in the covariance matrix as both θ and θ' rise suggests a correlation between these angular scales. Figure 7 provides a comprehensive view of how the BAO scale and its error (calculated by using Equation 15) evolve with redshift, emphasizing the impact of photo-z inaccuracies. The consistent relative error observed across measurements serves as a key finding, shedding light on the reliability of BAO scale determinations in the given redshift range. In future work on the application of this technique to data, one can estimate the covariance matrix from simulations.

Several detectors are set to measure the BAO scale with impressive accuracy, delving into the depths of the universe's redshift. Among these detectors, DESI (Adame et al. 2023) stands out as a ground-breaking 5-year experiment on the ground, specifically designed to investigate BAO and the changes in cosmic structures as seen through redshift-space distortions. Covering a vast area of 14,000 square degrees in the sky ($f_{sky} = 0.3$), DESI aims to achieve extremely precise measurements of the BAO feature. The goal is to surpass an impressive precision of 0.5%, focusing on redshift intervals $0.0 < z < 1.1$, $1.1 < z < 1.9$, and $1.9 < z < 3.7$ (Adame et al. 2023). Additionally, Euclid (Laureijs et al. 2011) and the Vera Rubin Observatory (Abell et al. 2009; Ivezić et al. 2019), covering a vast sky area of 18,000 square degrees will be able to make precise measurements of BAO up to high redshift.

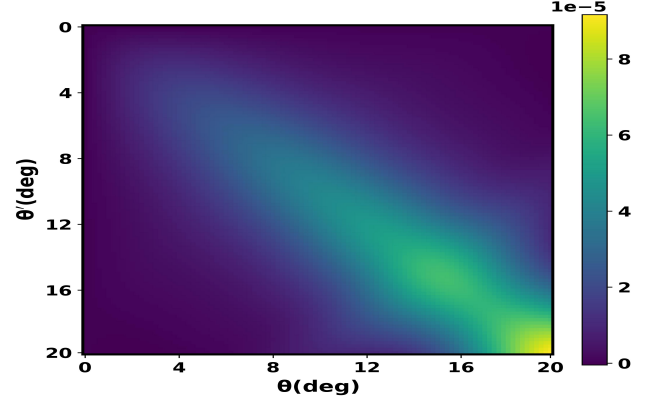


Figure 6. This plot displays the covariance matrix($Cov_{\theta\theta'}$) calculated using linear matter power spectrum as a function of θ and θ' for a specific redshift, $z=0.125$. It is evident that as both θ and θ' increase, the value of the covariance matrix also increases indicating larger error at the large angular scales.

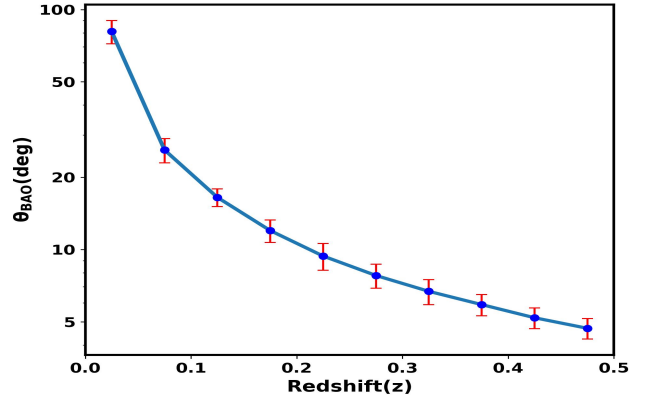


Figure 7. We depict the relationship between the BAO scale along with the associated error (in red), primarily arising from photo-z inaccuracies, as a function of redshift (z) up to $z = 0.5$. This presentation offers crucial insights into how the BAO scale and its error vary with z , highlighting a consistent relative error across measurements. For visual clarity, the error values on the plot have been magnified by a factor of 2.

5 FORECAST FOR RECONSTRUCTING \mathcal{F} WITH REDSHIFT

5.1 Case with the fixed Hubble constant H_0

The intricate connection between the EM wave luminosity distance at a specific redshift (z) and key cosmological parameters, including the BAO scale (θ_{BAO}) and the sound horizon (r_s), is succinctly captured by the equation

$$\mathcal{F}(z) = \frac{d_l^{GW}(z)\theta_{BAO}(z)}{(1+z)r_s}, \quad (20)$$

This equation serves as a focal point for the frictional component under consideration. In the context of ($\mathcal{F}(z)$), it establishes a connection with three distinct length scales (i) **GW luminosity distance**: The luminosity distance for detectable GW events which is determined using Bilby. (ii) **BAO scale**(θ_{BAO}): We utilize the BAO scale, derived from the 2PACF using the Equation 15. This method

is not bound to any particular survey, affording us the flexibility to apply our methodology across a range of surveys without being restricted to a specific one. (iii) **Sound Horizons distance**: The sound horizon is measured by analyzing acoustic oscillations in the CMB radiation using several missions such WMAP (Hinshaw et al. 2013), Planck (Aghanim et al. 2020), ACTPol (Thornton et al. 2016), SPT-3G (Sobrin et al. 2022), and CMB-S4 (Abazajian et al. 2016). In particular, the first peak observed in the angular power spectrum of the CMB corresponds to the scale of the sound horizon during the process of recombination. The measured sound horizon value at the drag epoch is found to be 147.09 ± 0.26 Mpc, indicating a high level of precision from Planck (Aghanim et al. 2020).

We utilize a Hierarchical Bayesian framework to calculate the posterior distribution of $\mathcal{F}(z)$ as a function of redshift for a total of n_{GW} GW sources. The equation representing the posterior distribution on $\mathcal{F}(z)$ for bright sirens is given as (Mukherjee et al. 2021a)

$$P(\mathcal{F}(z)|\{d^{GW}\}, \{z\}) \propto \Pi(\mathcal{F}(z)) \prod_{i=1}^{n_{GW}} \iiint dr_s P(r_s) dd_l^{GW^i} \\ \times d\theta_{BAO}^i P(\theta_{BAO}^i) \mathcal{L}(d_l^{GW^i} | \mathcal{F}(z^i), \theta_{BAO}^i, r_s, z^i), \quad (21)$$

In this equation, $P(\mathcal{F}(z)|\{d^{GW}\}, \{z\})$ denotes the posterior probability density function of $\mathcal{F}(z)$ given the GW source data d^{GW} and spectroscopic redshift from EM counterpart of these sources $\{z\}$ for $i \in n_{GW}$ events. The measurements of BAO angular scale θ_{BAO} at the redshift (z) of the GW source where an EM counterpart of GW source can be measured using the galaxy survey, and it is marginalized over. The term $\mathcal{L}(d_l^{GW^i} | \mathcal{F}(z^i), \theta_{BAO}^i, r_s, z^i)$ corresponds to the likelihood function. $P(r_s)$ and $P(\theta_{BAO}^i)$ denote the prior probability distributions for the sound horizon (r_s) and BAO scale respectively. The term $\Pi(\mathcal{F}(z))$ represents the prior distribution for $\mathcal{F}(z)$, which encapsulates our knowledge or assumptions about the frictional term before incorporating the measured data. We adopt a flat prior on the frictional term, $\mathcal{F}(z)$ from 0.1 to 2. For this investigation, we make specific assumptions regarding the probability distribution of redshift(z) and prior to the frictional term $\mathcal{F}(z)$. In this analysis, we consider bright sirens only. So, we assume that the host galaxy redshift of the GW sources is measured spectroscopically. In this case, it implies that we have precise knowledge or assume that the redshift of the sources is concentrated at a particular value.

In Figure 8, we presented the measurement of $\mathcal{F}(z)$, with a fixed value of H_0 for both the CE&ET and the LVK system, focusing on a single event. This plot illustrates a notable trend where the measurement error increases with higher redshifts. Additionally, it discerns that, at the same redshift, the error on $\mathcal{F}(z)$ is more pronounced for BNS systems compared to NSBH systems, attributed to the lower SNR observed for BNS events.

5.2 Case with varying the Hubble constant H_0

In the preceding sections, our analysis primarily focused on evaluating the frictional term denoted as $\mathcal{F}(z)$ in Equation 20, assuming a fixed Hubble constant (H_0). However, in this section, we jointly infer both $\mathcal{F}(z)$ and H_0 . This extension enables the simultaneous estimation of both the frictional term $\mathcal{F}(z)$ and H_0 , derived from sound horizon measurements that remain constant across redshift, serving as an overall normalization on $\mathcal{F}(z)$ measurements.

Employing a hierarchical Bayesian analysis, our unified framework efficiently estimates these two parameters by incorporating diverse

observational datasets, including GW measurements, CMB measurements, and large-scale structure surveys, as discussed in previous sections. The hierarchical organization of these datasets ensures robust integration, effectively handling their unique uncertainties and systematics. The resulting correlated constraints significantly contribute to our understanding of cosmological phenomena, addressing potential discrepancies between datasets and revealing insightful connections among fundamental cosmological parameters.

The equation representing the joint posterior distribution on $\mathcal{F}(z)$ and H_0 for these sources is given as (Mukherjee et al. 2021a)

$$P(\mathcal{F}(z), H_0 | \{d^{GW}\}, \{z\}) \propto \Pi(\mathcal{F}(z)) \Pi(H_0) \prod_{i=1}^{n_{GW}} \iiint \\ \times dr_s P(r_s) dd_l^{GW^i} d\theta_{BAO}^i P(\theta_{BAO}^i) \mathcal{L}(d_l^{GW^i} | \mathcal{F}(z^i), H_0, \theta_{BAO}^i, r_s, z^i), \quad (22)$$

In this equation, $P(\mathcal{F}(z), H_0 | \{d^{GW}\}, \{z\})$ denotes the joint posterior probability density Function of $\mathcal{F}(z)$ and H_0 . The term $\mathcal{L}(d_l^{GW^i} | \mathcal{F}(z^i), H_0, \theta_{BAO}^i, r_s, z^i)$ corresponds to the likelihood function. The term $\Pi(H_0)$ denotes the prior distribution for H_0 , encapsulating our knowledge or assumptions regarding the Hubble constant before incorporating measured data. All other terms represent the same entities as defined in Section 5.1. In our hierarchical Bayesian framework, we adopt a flat prior assumption, indicating a lack of prior knowledge about the parameters for both the frictional term ($\mathcal{F}(z)$) and the cosmic expansion rate (H_0). The parameter ranges are defined from 0.1 to 2.0 for $\mathcal{F}(z)$ and from 40 km/s/Mpc to 100 km/s/Mpc for H_0 .

In Figure 9, we present measurements of $\mathcal{F}(z)$ with varying values of H_0 for both the CE&ET and the LVK system, focusing on the total number of events within each redshift bin (mentioned in the parenthesis in the upper x-axis in the plot). This plot reveals a discernible trend, indicating an increase in measurement errors with higher redshifts. Notably, due to the higher likelihood of BNS events compared to NSBH events, we can achieve a more accurate measurement of $\mathcal{F}(z)$ for BNS events than for NSBH events.

6 RESULT

6.1 Reconstruction of $\mathcal{F}(z)$

This study exclusively focuses on bright sirens, indicating NSBH and BNS mergers with distinct EM counterparts (Nakar et al. 2018; Kasliwal et al. 2017; Arcavi 2018; Troja et al. 2017; Hallinan et al. 2017; Ghirlanda et al. 2019; Smartt et al. 2017; Kasen et al. 2017; Janka et al. 1999; Foucart 2012; Foucart et al. 2018). These include short GRBs and high-energy gamma-ray bursts detected by satellites like Fermi (Bissaldi et al. 2009) and Swift (Burrows et al. 2005). Additionally, kilonovae generate bright optical and infrared transients, offering insights into heavy element formation. Observatories like the Vera Rubin (Abell et al. 2009), HST (Scoville et al. 2007), and the upcoming Roman space telescope (Eifler et al. 2021) are poised to capture these events. Post-merger, afterglows spanning X-ray, UV, optical, and radio wavelengths are scrutinized with instruments such as Chandra (Vikhlinin et al. 2009), VLA Benz & Guedel (1989), ZTF (Bellm 2014), Astrosat (Agrawal 2006), Daksha (Bhalerao et al. 2022) and GMRT (Bhattacharyya et al. 2016).

Detecting EM counterparts in BNS and NSBH mergers poses challenges related to prompt collapse, ejecta mass, and orientation. The visibility of collimated jets is influenced by their opening angle,

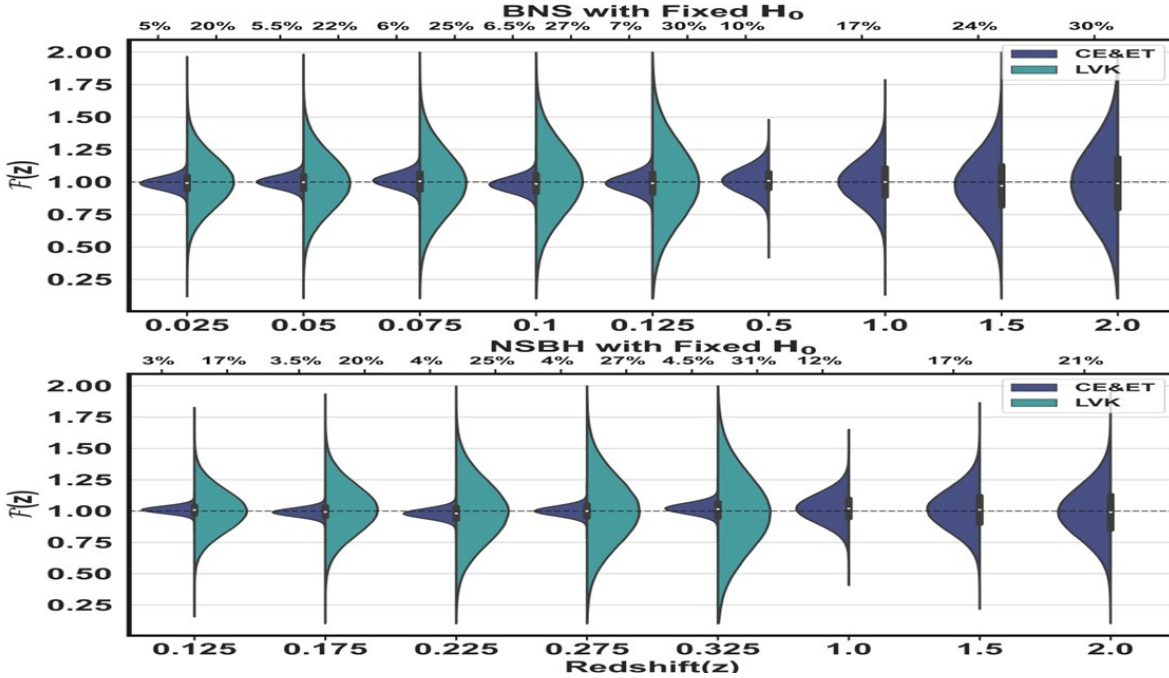


Figure 8. This violin plot illustrates the posterior on the reconstruction of the non-GR parameter $\mathcal{F}(z)$ as a function of cosmic redshift is feasible from LVK (in green) and CE&ET (in blue). The top and bottom plot relates to possible measurement using one BNS and NSBH source respectively, both assuming a fixed Hubble constant. The upper x-axis denotes the associated $1-\sigma$ error bars for each measurement. It demonstrates the potential to measure $\mathcal{F}(z)$ with greater precision and at significantly deeper cosmic redshifts using future detectors such as CE&ET, as opposed to the limitations of our current LVK detector.

with wider angles increasing detectability. Distance, instrument sensitivity, and rapid event localization further complicate detection. In astrophysics, terms like "structured jets" and "off-axis viewing" describe these phenomena (Rees & Mészáros 1998; Ramirez-Ruiz et al. 2001; Kumar & Piran 2000). Coordinated efforts between GW and EM observatories are vital for insights into these cosmic collisions. Despite progress, challenges persist, requiring proximity, orientation, and sensitivity considerations. Success relies on refining theoretical models, combining GW and EM observations, and technological advancements. Future endeavors aim to optimize multi-messenger observations, deepen theoretical comprehension, and amplify the detectability of NSBH merger EM counterparts.

In our study, we present cases for both the CE&ET and LVK systems. Specifically for CE&ET, we showcase outcomes for up to redshifts $z = 2$ for different numbers of detectable events. In the case of NSBH binaries, we consider a total of 30 events with a local merger rate (R_0) set at $20 \text{ Gpc}^{-3} \text{ yr}^{-1}$ in the LVK system. These events span redshifts from 0.125 to 0.425. Similarly, for BNS systems, we analyze approximately 25, 40, and 60 events with R_0 set to $200 \text{ Gpc}^{-3} \text{ yr}^{-1}$, $300 \text{ Gpc}^{-3} \text{ yr}^{-1}$, and $500 \text{ Gpc}^{-3} \text{ yr}^{-1}$, respectively. The redshifts of these events range from 0.025 to 0.225 over a 5-year observation period. In Figure 3 and Figure 4, the number of detectable events as a function of redshift with different R_0 and T_{obs} are presented for the LVK and CE&ET systems.

Figure 10 and Figure 11 provide a comprehensive comparison of $\mathcal{F}(z)$ measurements with fixed H_0 and varying H_0 across different scenarios for both LVK and CE&ET. These scenarios include the detection of a single event, a quarter of the events, half of the events, and the detection of all events. The aim is to demonstrate how the preci-

sion of measurements, ranging from percentages to sub-percentages, can be achieved using future detectors. This comparative analysis sheds light on the impact of event detection rates on the precision of $\mathcal{F}(z)$ measurements and underscores the potential of advanced detectors like CE&ET to provide increasingly accurate cosmological insights. In this section, we measure $\mathcal{F}(z)$ with a constant H_0 that remains uniform across redshifts, serving as an overall normalization factor for $\mathcal{F}(z)$ measurements. Consequently, if an independent precise measurement of $\mathcal{F}(z)$ in our local universe is possible, it will allow us to normalize it to 1, eliminating the dependence on H_0 . This normalization proves effective particularly for low redshifts, where the cumulative effects of modified gravity wave propagation have not had sufficient time to accumulate deviations from GR.

The error associated with the frictional term approximately scales as the inverse of the square root of the number of GW sources represented as $1/\sqrt{N_{\text{GW}}}$. This implies that as the number of GW sources increases, the error on the frictional term decreases, thereby improving the precision of the measurement. However, this improvement reaches a saturation point, beyond which an increase in the number of GW sources does not lead to a significant enhancement in the measurement's accuracy. This saturation is primarily due to the presence of error on the BAO scale. The BAO scale error acts as a limiting factor in the precision of the frictional term estimation. Therefore, to achieve further improvement in the estimation of the frictional term with redshift, a more precise measurement of the BAO scale is required. In essence, the precision of the frictional term estimation is a delicate balance between the number of GW sources and the accuracy of the BAO scale measurement and GW luminosity distance. Optimizing these factors can lead to significant advancements

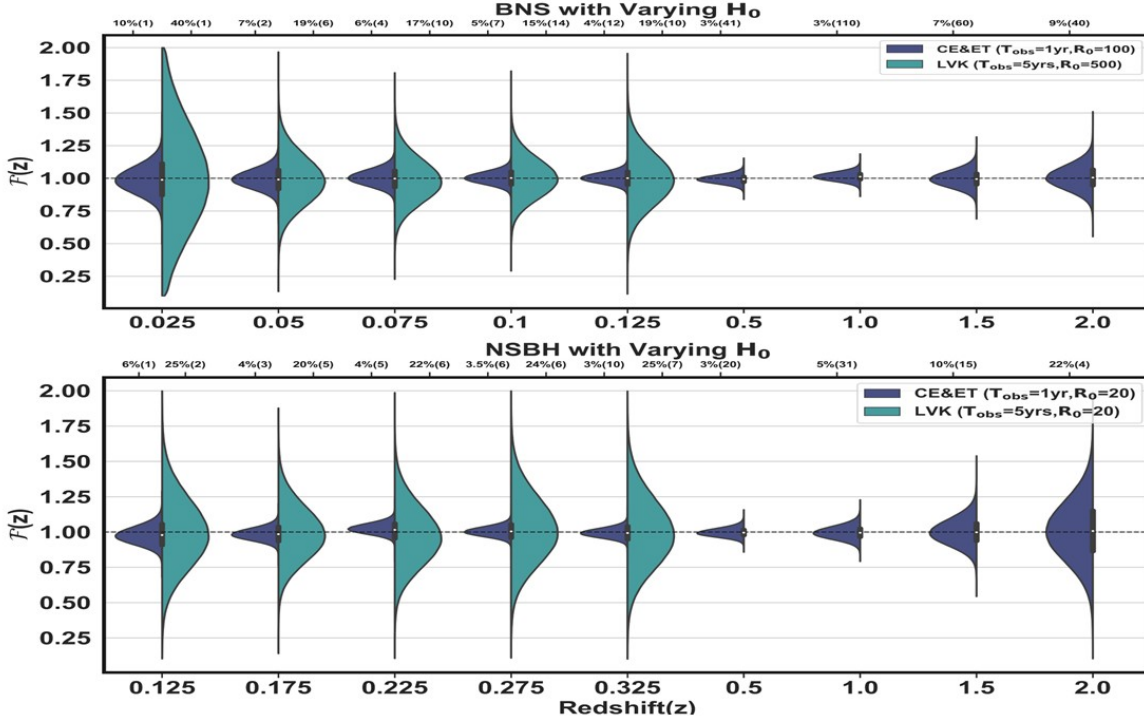


Figure 9. This violin plot illustrates the posterior on the reconstruction of the non-GR parameter $\mathcal{F}(z)$ as a function of cosmic redshift is feasible from LVK (in green) and CE&ET (in blue). The top and bottom plot relates to possible measurement using one BNS and NSBH source respectively jointly with the Hubble constant. The upper x-axis denotes the associated $1-\sigma$ error bars for each measurement, with the number in parentheses representing the total number of events in that specific redshift bin. The plot highlights the potential for more accurate measurements of $\mathcal{F}(z)$ at significantly deeper cosmic redshifts, particularly with future detectors like CE&ET, in contrast to the limitations posed by our current LVK detector, similar to the case with fixed Hubble constant. Additionally, it underscores that we can achieve more precise measurements of $\mathcal{F}(z)$ for BNS systems compared to NSBH events, given the higher likelihood of BNS events occurring.

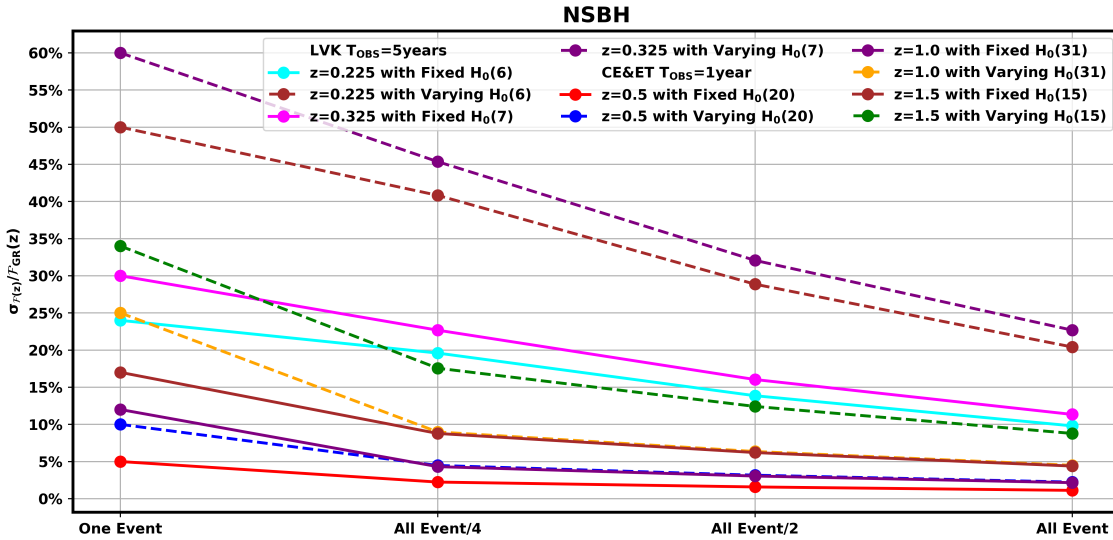


Figure 10. We show the $1-\sigma$ error-bar in the measurements of $\mathcal{F}(z)$ as a function of redshift and the number of GW events for NSBH events. The comparison is made between scenarios with a constant Hubble constant (H_0) and for the case with H_0 inferred jointly with $\mathcal{F}(z)$. All the events at each redshift bin are mentioned in parentheses in the figure legend.

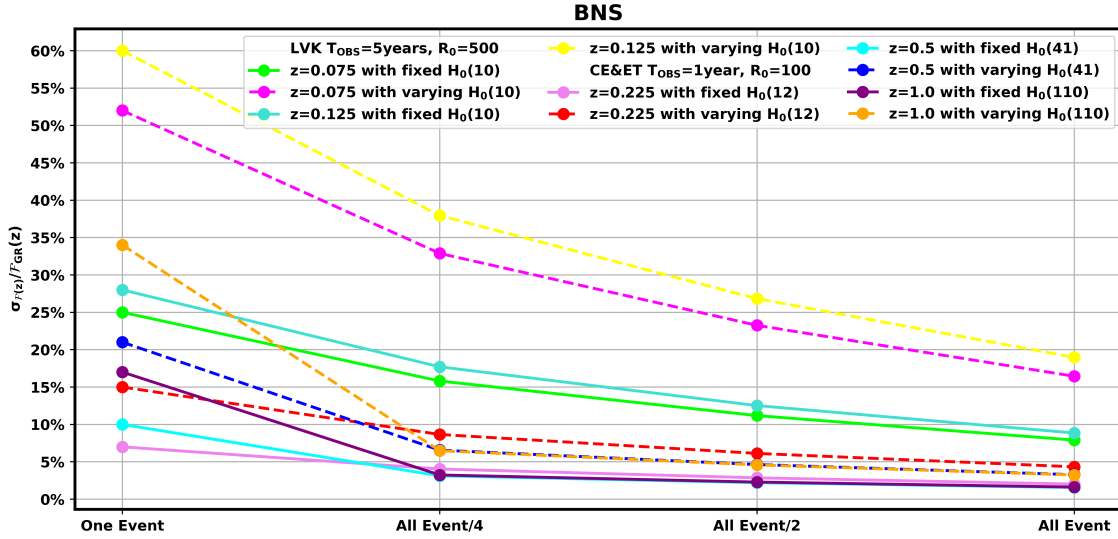


Figure 11. We show the 1- σ error-bar in the measurements of $\mathcal{F}(z)$ as a function of redshift and the number of GW events for BNS events. The comparison is made between scenarios with a constant Hubble constant (H_0) and those with varying H_0 . All the events at each redshift bin are mentioned in parentheses in the figure legend.

in our understanding of $\mathcal{F}(z)$ and discovering unexplored territories in fundamental physics. On the GW side, the measurements of $\mathcal{F}(z)$ are solely dependent on $d_l^{GW}(z)$. Any improvement in the precision of $d_l^{GW}(z)$ will markedly enhance the accuracy of $\mathcal{F}(z)$, as $d_l^{GW}(z)$ stands out as the predominant source of error for $\mathcal{F}(z)$. Given that $d_l^{GW}(z)$ is degenerate with other GW parameters, most notably the inclination angle (i), measuring inclination angle from alternative sources (such as EM counterparts) can substantially reduce the error in $d_l^{GW}(z)$ and consequently enhance the precision of $\mathcal{F}(z)$ (Xie et al. 2023). For redshift inference from EM counterparts, the influence of peculiar velocity contamination is particularly significant at low redshifts ($z < 0.03$) but it is not important for high redshift (Mukherjee et al. 2021b; Nimonkar & Mukherjee 2024). As most of the detected sources are at high redshift, we have ignored this effect. Also, weak lensing of the GW sources can be a source of contamination to the luminosity distance up to a few percent at redshifts above $z = 0.5$ (Hirata et al. 2010). In comparison to the error bar on luminosity distance, the weak lensing error bar is small. As most of the sources with better luminosity distance measurement are mainly at low redshift ($z < 0.5$), we are getting maximum constraints around this redshift. So, the weak lensing uncertainty is not a major contamination for these sources. Moreover, weak lensing can provide additional information to constraint non-GR parameter space (Mukherjee et al. 2020a,b; Mpetha et al. 2023; Balaudo et al. 2023), which we have not considered in this analysis.

6.2 Reconstruction of $\mathcal{F}(z)$ and H_0

By extension of the hierarchical Bayesian framework used in the previous section to measure $\mathcal{F}(z)$ with fixed H_0 , we can jointly measure $\mathcal{F}(z)$ and H_0 . In our framework, we measure the EM luminosity distance from different length scales, namely the BAO scale, sound horizon distance, and redshift. In Figure 10 and Figure 11, we offer a thorough comparison of $\mathcal{F}(z)$ measurements with both fixed and

varying H_0 across different scenarios for both the LVK and CE&ET systems. It is noteworthy that when allowing for variations in H_0 , the errors in the measurements of $\mathcal{F}(z)$ increased by a factor ranging from 2 to 2.2 compared to measurements with a fixed H_0 . In Figure 1, we highlight the enhanced precision in measuring the redshift-dependent variation of the Planck mass ($\mathcal{F}(z)$) for NSBH and BNS systems. The figure emphasizes that the measurement of $\mathcal{F}(z)$ is notably improved in the redshift range of 0.2 to 1.0. The precision of estimating $\mathcal{F}(z)$ depends on accurate measurements of both the BAO scale and $d_l^{GW}(z)$. Improved accuracy in the BAO scale measurements directly enhances precision in estimating $\mathcal{F}(z)$. On the GW side, accurate measurements of $\mathcal{F}(z)$ rely solely on $d_l^{GW}(z)$. Enhancing the precision of $d_l^{GW}(z)$ improves $\mathcal{F}(z)$, as mentioned in the previous Subsection 6.1. There can also be peculiar velocity corrections and weak lensing contamination at low redshift as described in 6.1 which are not taken care of in this study.

7 CONCLUSION AND DISCUSSION

In this study, we present a model-independent approach to search for the frictional term, which can capture deviations at any redshift from GR. We propose a model-independent reconstruction of the frictional term as a function of redshift using a data-driven approach by amalgamating three length scales with redshift namely the luminosity distance from GW sources $d_l^{GW}(z)$, the angular scale of BAO scale from galaxy surveys $\theta_{BAO}(z)$, and the sound horizon r_s from CMB observations. We show this provides a unique opportunity to scrutinize theories of gravity, specifically to test the presence of a frictional term. In the literature, various model-dependent searches for the frictional term have been conducted. These searches face challenges, especially near redshift $z=0$ and at large redshifts. Particularly noteworthy are the difficulties encountered when there is a potential loss of gravitons in extra dimensions. Furthermore, in the interme-

diate redshift range, the frictional term may display oscillatory behavior that cannot be adequately captured by these model-dependent searches.

We demonstrate that by integrating BAO measurements from galaxies, sound horizon distances from the CMB power spectrum, redshift information from the EM counterpart, and luminosity distance measurements from GW sources, one can perform a comprehensive measurement of cosmological parameters. Specifically, we highlight the potential to jointly determine the Hubble constant (H_0) and the frictional term through this integrated analysis. We have demonstrated the feasibility of measuring the frictional term using our ongoing detectors, such as LVK, across various redshifts. Additionally, we have explored the capabilities of upcoming detectors, specifically CE&ET, in quantifying the frictional term under various scenarios. Our analysis includes cases where a fraction of the event's EM counterpart is detectable, acknowledging the inherent difficulty in detecting EM counterparts.

We demonstrate the feasibility of achieving a precision measurement of the frictional term, ranging from a percent to sub-percent accuracy, as a function of cosmic redshift. This is achievable using data from LVK and, in the future, from CE&ET, despite the limitation of a finite number of bright sirens. The measurement of $\mathcal{F}(z)$ is particularly improved in the redshift range of 0.2 to 1.0. This improvement is attributed to two main factors: SNR and the number of events. The measurements from LVK can be further improved by including LIGO-India (Saleem et al. 2021)³.

In the (Ξ_0, n) parametrizations of the frictional term, the fiducial value for Ξ_0 is set to 1. However, it is important to note that the parameter n is not defined at this fiducial value of $\Xi_0=1$. Consequently, measuring the value of n becomes increasingly challenging as Ξ_0 approaches 1 (Belgacem et al. 2018b). By utilizing 1000 bright sirens up to redshift 8, Belgacem et al. (2018b) demonstrated that Ξ_0 can be measured with an accuracy of 0.8% using the Einstein Telescope for a fixed value of n . In our study, employing a model-independent parametrization, we found that with 1 year of observation using CE&ET, we can measure the frictional term with an accuracy of 1.62% and 2% for BNS and NSBH systems at redshift 0.5. Additionally, we can reconstruct the frictional term as a function of redshift without relying on any specific parametrization, as illustrated in Figure 1. This error scales inversely with the square root of the observation time, i.e., as $1/\sqrt{T_{obs}/years}$.

Our proposed technique extends to dark sirens, where redshift inference becomes necessary. In such cases, we leverage the three-dimensional clustering scale of GW sources with galaxies to infer redshift information (Mukherjee & Wandelt 2018; Mukherjee et al. 2020c; Abbott et al. 2021). Furthermore, this methodology holds promise for both bright and dark standard sirens in the mHz range, detectable by future space-based detectors like LISA. In this study, our exclusive focus is on bright sirens, and as a result, we exclude a prominent category of GW sources Binary Black Holes (BBH) due to their unlikely association with EM counterparts. Additionally, there are challenges associated with detecting EM counterparts for BNS and NSBH systems (Chase et al. 2022; Ronchini et al. 2022). One potential method to enhance the accuracy of frictional term measurements is to include dark sirens, which lack EM counterparts. In future, the integration of LIGO-India and the LISA GW detector, in conjunction with projects such as eBOSS, DESI, Vera Rubin, and Euclid for BAO measurements, along with the application of this

technique to dark sirens, holds the potential to substantially improve the precision of measuring the frictional term.

ACKNOWLEDGEMENTS

The authors express their gratitude to Guillaume Dideron for reviewing the manuscript and providing useful comments as a part of the LIGO publication policy. This work is part of the `<data|theory>` Universe-Lab, supported by TIFR and the Department of Atomic Energy, Government of India. The authors express gratitude to the computer cluster `<data|theory>` Universe-Lab and the TIFR computer center HPC facility for computing resources. Special thanks to the LIGO-Virgo-KAGRA Scientific Collaboration for providing noise curves. LIGO, funded by the U.S. National Science Foundation (NSF), and Virgo, supported by the French CNRS, Italian INFN, and Dutch Nikhef, along with contributions from Polish and Hungarian institutes. This collaborative effort is backed by the NSF's LIGO Laboratory, a major facility fully funded by the National Science Foundation. The research leverages data and software from the Gravitational Wave Open Science Center, a service provided by LIGO Laboratory, the LIGO Scientific Collaboration, Virgo Collaboration, and KAGRA. Advanced LIGO's construction and operation receive support from STFC of the UK, Max-Planck Society (MPS), and the State of Niedersachsen/Germany, with additional backing from the Australian Research Council. Virgo, affiliated with the European Gravitational Observatory (EGO), secures funding through contributions from various European institutions. Meanwhile, KAGRA's construction and operation are funded by MEXT, JSPS, NRF, MSIT, AS, and MOST.

This material is based upon work supported by NSF's LIGO Laboratory which is a major facility fully funded by the National Science Foundation. We acknowledge the use of the following packages in this work: Astropy (Robitaille et al. 2013; Price-Whelan et al. 2018), Bilby (Ashton et al. 2019), Pandas (McKinney et al. 2011), NumPy (Harris et al. 2020), Seaborn (Bisong & Bisong 2019), CAMB (Lewis & Challinor 2011), Scipy (Virtanen et al. 2020), Matplotlib (Hunter 2007), Dynesty (Speagle 2020), and emcee (Foreman-Mackey et al. 2013)

DATA AVAILABILITY

The corresponding author will provide the underlying data for this article upon request.

REFERENCES

- Aasi J., et al., 2015, Classical and quantum gravity, 32, 074001
- Abazajian K. N., et al., 2016, arXiv preprint arXiv:1610.02743
- Abbott B. P., et al., 2016a, Physical Review X, 6, 041015
- Abbott B. P., et al., 2016b, Physical review letters, 116, 061102
- Abbott B. P., et al., 2016c, Physical review letters, 116, 241103
- Abbott B. P., et al., 2017a, Physical review letters, 119, 161101
- Abbott B. P., et al., 2017b, The Astrophysical Journal Letters, 848, L13
- Abbott B. P., et al., 2019a, Physical review letters, 123, 011102
- Abbott B., et al., 2019b, The Astrophysical Journal Letters, 882, L24
- Abbott R., et al., 2021, arXiv preprint arXiv:2111.03604
- Abbott R., et al., 2023, Physical Review X, 13, 011048
- Abell P. A., et al., 2009, arXiv preprint arXiv:0912.0201
- Abitbol M. H., et al., 2019, arXiv preprint arXiv:1907.08284
- Acernese F. a., et al., 2014, Classical and Quantum Gravity, 32, 024001
- Achour J. B., Langlois D., Noui K., 2016, Physical Review D, 93, 124005

³ <https://dcc.ligo.org/LIGO-M1100296/public>

- Adame A., et al., 2023, arXiv preprint arXiv:2306.06308
- Aghanim N., et al., 2020, *Astronomy & Astrophysics*, 641, A6
- Agrawal P., 2006, *Advances in Space Research*, 38, 2989
- Ajith et al., 2008, *Physical Review D*, 77, 104017
- Akutsu T., et al., 2021, *Progress of Theoretical and Experimental Physics*, 2021, 05A101
- Alam S., et al., 2017, *Monthly Notices of the Royal Astronomical Society*, 470, 2617
- Amaro-Seoane P., et al., 2017, arXiv preprint arXiv:1702.00786
- Anderson L., et al., 2012, *Monthly Notices of the Royal Astronomical Society*, 427, 3435
- Arcavi I., 2018, *The Astrophysical Journal Letters*, 855, L23
- Ashton G., et al., 2019, *The Astrophysical Journal Supplement Series*, 241, 27
- Baker T., Harrison I., 2021, *JCAP*, 01, 068
- Balasubramanian R., Sathyaprakash B. S., Dhurandhar S., 1996, *Physical Review D*, 53, 3033
- Balaudo A., Garoffolo A., Martinelli M., Mukherjee S., Silvestri A., 2023, *Journal of Cosmology and Astroparticle Physics*, 2023, 050
- Belgacem E., Dirian Y., Foffa S., Maggiore M., 2018a, *Physical review D*, 97, 104066
- Belgacem E., Dirian Y., Foffa S., Maggiore M., 2018b, *Physical review D*, 98, 023510
- Belgacem E., et al., 2019, *Journal of Cosmology and Astroparticle Physics*, 2019, 024
- Bellm E., 2014, in *The Third Hot-wiring the Transient Universe Workshop*.
- Benz A., Guedel M., 1989, *Astronomy and Astrophysics* (ISSN 0004-6361), vol. 218, no. 1-2, July 1989, p. 137–140., 218, 137
- Bhalerao V., et al., 2022, arXiv preprint arXiv:2211.12052
- Bhattacharyya B., et al., 2016, *The Astrophysical Journal*, 817, 130
- Bisong E., Bisong E., 2019, *Building Machine Learning and Deep Learning Models on Google Cloud Platform: A Comprehensive Guide for Beginners*, pp 151–165
- Bissaldi E., et al., 2009, *Experimental Astronomy*, 24, 47
- Blake C., Glazebrook K., 2003, *The Astrophysical Journal*, 594, 665
- Bond J., Efstathiou G., 1987, *Monthly Notices of the Royal Astronomical Society*, 226, 655
- Brans C., Dicke R. H., 1961, *Physical review*, 124, 925
- Burrows D. N., et al., 2005, *Space science reviews*, 120, 165
- Cabré A., Fosalba P., Gaztanaga E., Manera M., 2007, *Monthly Notices of the Royal Astronomical Society*, 381, 1347
- Cai Y.-F., Capozziello S., De Laurentis M., Saridakis E. N., 2016, *Reports on Progress in Physics*, 79, 106901
- Carvalho G., Bernui A., Benetti M., Carvalho J., Alcaniz J., 2016, *Physical Review D*, 93, 023530
- Chase E. A., et al., 2022, *The Astrophysical Journal*, 927, 163
- Chow N., Khouri J., 2009, *Physical Review D*, 80, 024037
- Corman M., Escamilla-Rivera C., Hendry M., 2021, *Journal of Cosmology and Astroparticle Physics*, 2021, 005
- Crisostomi M., Koyama K., Tasinato G., 2016, *Journal of Cosmology and Astroparticle Physics*, 2016, 044
- Crocce M., Cabré A., Gaztanaga E., 2011, *Monthly Notices of the Royal Astronomical Society*, 414, 329
- Cutler C., Flanagan E. E., 1994, *Physical Review D*, 49, 2658
- Davis M., Peebles P., 1983, *Astrophysical Journal*, Part 1 (ISSN 0004-637X), vol. 267, April 15, 1983, p. 465–482., 267, 465
- De Felice A., Larrouturou F., Mukohiyama S., Oliosi M., 2021, *Journal of Cosmology and Astroparticle Physics*, 2021, 015
- Deffayet C., Menou K., 2007, *The Astrophysical Journal*, 668, L143
- Dodelson S., Schmidt F., 2020, *Modern cosmology*. Academic press
- Dominik M., et al., 2015, *The Astrophysical Journal*, 806, 263
- Doré O., et al., 2018, arXiv preprint arXiv:1805.05489
- Dvali G., Gabadadze G., Porrati M., 2000, *Physics Letters B*, 485, 208
- Eifler T., et al., 2021, *Monthly Notices of the Royal Astronomical Society*, 507, 1746
- Finn L. S., 1996, *Physical Review D*, 53, 2878
- Finn L. S., Chernoff D. F., 1993, *Physical Review D*, 47, 2198
- Foreman-Mackey D., Hogg D. W., Lang D., Goodman J., 2013, *Publications of the Astronomical Society of the Pacific*, 125, 306
- Foucart F., 2012, *Physical Review D*, 86, 124007
- Foucart F., Hinderer T., Nissanke S., 2018, arXiv preprint arXiv:1807.00011
- Frusciante N., Kase R., Koyama K., Tsujikawa S., Vernieri D., 2019, *Physics Letters B*, 790, 167
- Ghirlanda G., et al., 2019, *Science*, 363, 968
- Goldstein A., et al., 2017, *The Astrophysical Journal Letters*, 848, L14
- Hallinan G., et al., 2017, *Science*, 358, 1579
- Hamilton A., 1993, *The Astrophysical Journal*, 417, 19
- Harris C. R., et al., 2020, *Nature*, 585, 357
- Hewett P. C., 1982, *Monthly Notices of the Royal Astronomical Society*, 201, 867
- Hinshaw G., et al., 2013, *The Astrophysical Journal Supplement Series*, 208, 19
- Hirata C. M., Holz D. E., Cutler C., 2010, *Phys. Rev. D*, 81, 124046
- Hu W., Dodelson S., 2002, *Annual Review of Astronomy and Astrophysics*, 40, 171
- Hu W., Sawicki I., 2007, *Physical Review D*, 76, 064004
- Hunter J. D., 2007, *Computing in Science & Engineering*, 9, 90
- Ivezić Ž., et al., 2019, *The Astrophysical Journal*, 873, 111
- Janka H.-T., Eberl T., Ruffert M., Fryer C. L., 1999, *The Astrophysical Journal*, 527, L39
- Kalaghatgi C., Hannam M., Raymond V., 2020, *Physical Review D*, 101, 103004
- Karathanasis et al., 2022, arXiv preprint arXiv:2210.05724
- Karathanasis C., Mukherjee S., Mastrogianni S., 2023, *Monthly Notices of the Royal Astronomical Society*, 523, 4539
- Kasen D., Metzger B., Barnes J., Quataert E., Ramirez-Ruiz E., 2017, *Nature*, 551, 80
- Kasliwal M., et al., 2017, *Science*, 358, 1559
- Komatsu E., et al., 2011, arXiv preprint arXiv:1001.4635
- Kumar P., Piran T., 2000, *The Astrophysical Journal*, 532, 286
- Landy S. D., Szalay A. S., 1993, *Astrophysical Journal*, Part 1 (ISSN 0004-637X), vol. 412, no. 1, p. 64–71., 412, 64
- Laureijs R., et al., 2011, arXiv preprint arXiv:1110.3193
- Lewis A., Challinor A., 2011, *Astrophysics source code library*, pp ascl–1102
- Leyde K., Mastrogianni S., Steer D. A., Chassande-Mottin E., Karathanasis C., 2022, *Journal of Cosmology and Astroparticle Physics*, 2022, 012
- Lombbriser L., Lima N. A., 2017, *Physics Letters B*, 765, 382
- Lombbriser L., Taylor A., 2016, *Journal of Cosmology and Astroparticle Physics*, 2016, 031
- Madau P., Dickinson M., 2014, *Annual Review of Astronomy and Astrophysics*, 52, 415
- Maggiore M., 2007, *Gravitational waves: Volume 1: Theory and experiments*. OUP Oxford
- Mandelbaum R., et al., 2018, arXiv preprint arXiv:1809.01669
- McKinney W., et al., 2011, *Python for high performance and scientific computing*, 14, 1
- Mpetha C. T., Congedo G., Taylor A., 2023, *Phys. Rev. D*, 107, 103518
- Mukherjee S., Wandelt B. D., 2018, arXiv preprint arXiv:1808.06615
- Mukherjee S., Wandelt B. D., Silk J., 2020a, *Physical Review D*, 101, 103509
- Mukherjee S., Wandelt B. D., Silk J., 2020b, *Mon. Not. Roy. Astron. Soc.*, 494, 1956
- Mukherjee S., Wandelt B. D., Silk J., 2020c, *Monthly Notices of the Royal Astronomical Society*, 494, 1956
- Mukherjee S., et al., 2021a, *Monthly Notices of the Royal Astronomical Society*, 502, 1136
- Mukherjee S., Lavaux G., Bouchet F. R., Jasche J., Wandelt B. D., Nissanke S. M., Leclercq F., Hotokezaka K., 2021b, *Astron. Astrophys.*, 646, A65
- Nakar E., Gottlieb O., Piran T., Kasliwal M. M., Hallinan G., 2018, *The Astrophysical Journal*, 867, 18
- Nimonkar H., Mukherjee S., 2024, *Monthly Notices of the Royal Astronomical Society*, 527, 2152
- Nishizawa A., 2018, *Physical Review D*, 97, 104037
- Nissanke S., Holz D. E., Hughes S. A., Dalal N., Sievers J. L., 2010, *The Astrophysical Journal*, 725, 496
- Ochsner E., Wisconsin-Milwaukee U., Nepal P., Qi H., 2012, *ApJ*, 746, 186

- Peebles P., 1973, *Astrophysical Journal*, Vol. 185, pp. 413-440 (1973), 185, 413
- Peebles P. J. E., Hauser M. G., 1974, *The Astrophysical Journal Supplement Series*, 28, 19
- Peebles P. J., Yu J., 1970, *The Astrophysical Journal*, 162, 815
- Price-Whelan A. M., et al., 2018, *The Astronomical Journal*, 156, 123
- Punturo M., et al., 2010, *Classical and Quantum Gravity*, 27, 194002
- Ramirez-Ruiz E., Merloni A., Rees M. J., 2001, *Monthly Notices of the Royal Astronomical Society*, 324, 1147
- Rees M., Mészáros P., 1998, *The Astrophysical Journal*, 496, L1
- Reitze D., et al., 2019, arXiv preprint arXiv:1907.04833
- Robitaille T. P., et al., 2013, arXiv preprint arXiv:1307.6212
- Ronchini S., et al., 2022, *Astron. Astrophys.*, 665, A97
- Saleem M., et al., 2021, *Classical and Quantum Gravity*, 39, 025004
- Saltas I. D., Sawicki I., Amendola L., Kunz M., 2014, *Physical Review Letters*, 113, 191101
- Sathyaprakash B. S., Dhurandhar S., 1991, *Physical Review D*, 44, 3819
- Sathyaprakash B. S., Schutz B. F., 2009, *Living reviews in relativity*, 12, 1
- Scientific L., et al., 2017, *Physical review letters*, 118, 221101
- Scoville N., et al., 2007, *The Astrophysical Journal Supplement Series*, 172, 38
- Smartt S., et al., 2017, *Nature*, 551, 75
- Sobrin J., et al., 2022, *The Astrophysical Journal Supplement Series*, 258, 42
- Speagle J. S., 2020, *Monthly Notices of the Royal Astronomical Society*, 493, 3132
- Spergel D. N., et al., 2007, *The astrophysical journal supplement series*, 170, 377
- Sunyaev R. A., Zeldovich Y. B., 1970, *Astrophysics and Space Science*, 7, 3
- Talbot C., Thrane E., 2018, *The Astrophysical Journal*, 856, 173
- Thorne K. S., 1995, arXiv preprint gr-qc/9506086
- Thornton R., et al., 2016, *The Astrophysical Journal Supplement Series*, 227, 21
- Troja E., et al., 2017, *Nature*, 551, 71
- Vikhlinin A., et al., 2009, *The Astrophysical Journal*, 692, 1060
- Virtanen P., et al., 2020, *Zenodo*
- Xie Y., Chatterjee D., Holder G., Holz D. E., Perkins S., Yagi K., Yunes N., 2023, *Physical Review D*, 107, 043010
- Xu X., Padmanabhan N., Eisenstein D. J., Mehta K. T., Cuesta A. J., 2012, *Monthly Notices of the Royal Astronomical Society*, 427, 2146
- Yamashita Y., Tanaka T., 2014, *Journal of Cosmology and Astroparticle Physics*, 2014, 004

APPENDIX A: UNCERTAINTIES IN H_0 IN THE RECONSTRUCTION OF H_0 AND $\mathcal{F}(Z)$

In Section 6.2, we extended the hierarchical Bayesian framework previously employed for measuring $\mathcal{F}(z)$ with a fixed H_0 to a joint measurement scenario for both $\mathcal{F}(z)$ and H_0 . Within this framework, a flat prior assumption was utilized, indicating a lack of prior knowledge about the parameters associated with the frictional term ($\mathcal{F}(z)$) and the cosmic expansion rate (H_0). For the parameters governing the frictional term ($\mathcal{F}(z)$) and the Hubble constant (H_0), we established parameter ranges of 0.1 to 2.0 and 40 km/s/Mpc to 100 km/s/Mpc, respectively.

In Figure A1, we showcase the joint posterior of $\mathcal{F}(z)$ and H_0 for two distinct scenarios. The first scenario corresponds to CE&ET, considering all observed events for $z=0.225$ in the case of NSBH events. The second scenario pertains to LVK, also for $z=0.225$ also focusing on NSBH events. This visualization provides a comparative analysis, illustrating the potential advancements achievable with our future detector, CE&ET, in contrast to the current capabilities of the LVK detector. The joint posterior distribution offers valuable insights into the precision and capabilities of each detector in estimating the parameters $\mathcal{F}(z)$ and H_0 . In Figure A2 and Figure A3 we showed

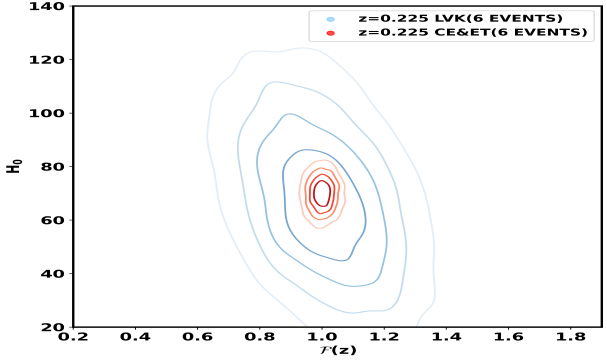


Figure A1. In this plot, we depict the joint posterior of $\mathcal{F}(z)$ and H_0 for CE&ET and LVK for the NSBH events for a total number of events scenario at $z=0.225$. In the parenthesis, it depicts the total no of events at that particular redshift.

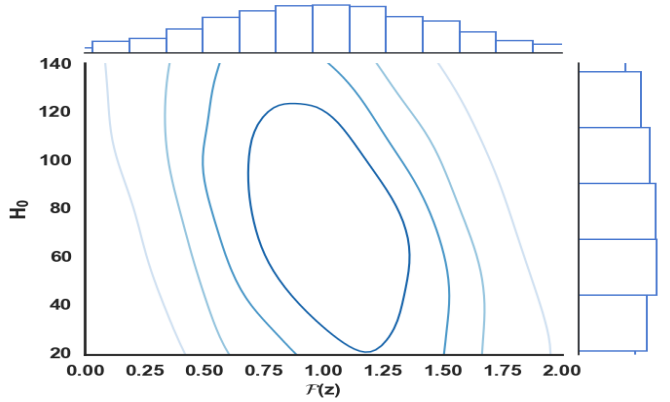


Figure A2. In this plot, we depict the Joint Posterior of $\mathcal{F}(z)$ and H_0 upto 4 σ level for LVK for the NSBH events scenario at $z=0.225$ for one event.

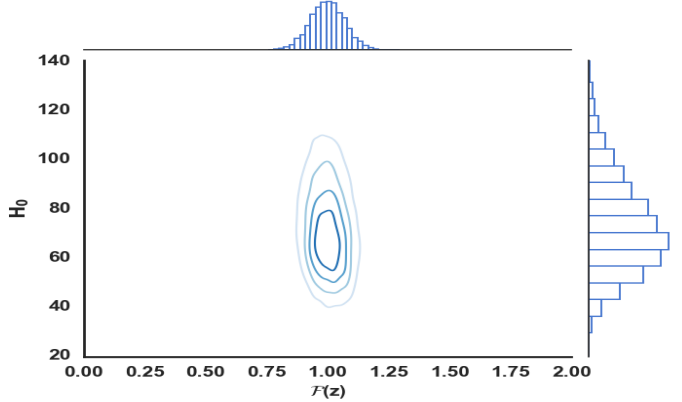


Figure A3. In this plot, we depict the joint posterior of $\mathcal{F}(z)$ and H_0 upto 4 σ level for CE&ET for the NSBH events scenario at $z=0.225$ for one event. the joint posterior of $\mathcal{F}(z)$ and H_0 for CE&ET and LVK at redshift 0.225 for just only one event.